Electronic Supplementary Information

Integration of thermo-electrochemical conversion into forced convection cooling

Yutaka Ikeda, Kazuki Fukui and Yoichi Murakami*

School of Engineering, Tokyo Institute of Technology, 2-12-1 Ookayama, Meguro-ku, Tokyo 152-8552, Japan

*Corresponding Author: Yoichi Murakami, E-mail: murakami.y.af@m.titech.ac.jp

List of Contents

1. Derivation of the rate of exergy loss

As a result of the second law of thermodynamics, the thermal energy of E_{therm} (J) located in a heat-releasing object at T_{obj} (K) has an exergy ($E_{\mathrm{X,obj}}$ (J)) of[S1]

$$E_{\mathrm{X,obj}} = E_{\mathrm{therm}}\left(1 - \frac{T_{\mathrm{env}}}{T_{\mathrm{obj}}}\right), \tag{S1}$$

where T_{env} is the temperature of the environment (~300 K). Similarly, the exergy of the same amount of thermal energy when it is located in the coolant liquid at the temperature T_{liq} (K), denoted $E_{\mathrm{X,liq}}$ (J), is

$$E_{\mathrm{X,liq}} = E_{\mathrm{therm}}\left(1 - \frac{T_{\mathrm{env}}}{T_{\mathrm{liq}}}\right). \tag{S2}$$

Therefore, the exergy loss caused by the transfer of E_{therm} as a heat Q (i.e., $Q = E_{\mathrm{therm}}$) from the heat-releasing object to the coolant liquid is equal to

$$E_{\mathrm{X,obj}} - E_{\mathrm{X,liq}} = Q\left(\frac{T_{\mathrm{env}}}{T_{\mathrm{liq}}} - \frac{T_{\mathrm{env}}}{T_{\mathrm{obj}}}\right) = Q\frac{T_{\mathrm{env}}}{T_{\mathrm{liq}}T_{\mathrm{obj}}}\left(T_{\mathrm{obj}} - T_{\mathrm{liq}}\right). \tag{S3}$$

To make this equation a per-unit-time representation, Q (J) is replaced by $\dot{Q}$ (J/s). Thus, the rate of exergy loss, $E_{\mathrm{X,loss}}$ (J/s), is expressed as

$$E_{\mathrm{X,loss}} = \dot{Q}\frac{T_{\mathrm{env}}}{T_{\mathrm{liq}}T_{\mathrm{obj}}}\left(T_{\mathrm{obj}} - T_{\mathrm{liq}}\right) \propto \dot{Q}\left(T_{\mathrm{obj}} - T_{\mathrm{liq}}\right), \tag{S4}$$

which is the relationship used in Section 1 of the main text.

2. Experimental details

Preparation of the working liquid

The preparation, handling, and storage of the working liquid (0.06 M solution of $Co^{II/III}(bpy)_3(NTf_2)_{2/3}$ in $[C_2mim][NTf_2]$) were carried out in a glovebox equipped with a circulation gas purifier (OMNI-LAB, Vacuum Atmospheres Company). In this glovebox, the moisture and oxygen concentrations were kept below 1 ppm. First, as-received $[C_2mim][NTf_2]$

was dried under vacuum at 110 °C for 3 h in an open glass vessel with the liquid surface height below ca. 5 mm to facilitate the escape of moisture. The powders of $Co^{II}(bpy)_3(NTf_2)_2$ and $Co^{III}(bpy)_3(NTf_2)_3$ were then dissolved in $[C_2mim][NTf_2]$ in an open-top glass bottle by stirring the mixture on a hot-plate stirrer at 50 °C for 15 h. This process was conducted in the glovebox to further remove moisture from the liquid. The complete dissolution of the redox couple was checked by irradiating the liquid with a laser beam (wavelength: 632.8 nm), which confirmed the absence of light scattering from powder particles. This check was also performed before and after each experiment to confirm that the redox species did not precipitate from the solution. The working liquid was stored in the dark in the glovebox. Just before the experiment, the liquid was degassed in a vacuum oven at 50 °C for about 40 min. We found that this degassing treatment was important to prevent the emergence of gas bubbles during experiments.

Liquid circulation and flow rate measurement

The working liquid was circulated using a roller tubing pump (Masterflex, Cole-Parmer) equipped with a PTFE-tubing pump head (HV-77390-00, Cole-Parmer). The liquid flow rate was modulated by the rotation speed of the head. The actual flow rate or G was measured for each experiment by introducing an air plug into the loop from a manifold junction in the middle of the loop and recording a digital movie to determine the progression rate of the air plug.

Fabrication and treatment of the electrodes

The anode was processed from a Pt plate (thickness: 0.3 mm; purity: > 99.98%) to dimensions of 29.5 × 25 mm for the directions parallel and perpendicular to the flow, respectively, by discharge cutting using an electrical wire. Cathode #1–3 (cf. Fig. 3c in the main text) were fabricated by

machine processing of a nickel block (purity: > 99.8%). The surfaces of the cathodes were sputter-coated with a Pt layer with a thickness of 100–130 nm to form a reversible electrode. Before each experiment, the anode was polished using a water slurry of alumina powder, rinsed with ultra-high purity water with a resistance of 18.2 MΩ·cm, and dried well in an oven at 70 °C. After each series of experiments, the cell was deconstructed and the electrodes were carefully cleaned by repeated ultrasonication first in acetone and then in methanol. Using these electrode treatments, we attained data reproducibility within 5%.

Heater and temperature control

The temperature of the cathode was set at a target value using a ceramic heater (BVP-004, Bach Resistor Ceramics GmbH, Germany) tightly contacted with the top plane of the cathode (cf. Fig. 3b in the main text). The heater body was composed of silicon nitride with dimensions of 18 × 18 × 3 mm. A sheathed thermocouple with a diameter of 1 mm was embedded inside the ceramic heater and this output was used for fast feedback control at a frequency of 50 Hz. The electric power consumption by the heater was measured in each experiment using a power meter (Model 3333, Hioki, Japan). This value was used to calculate the amount of Q (see below). T_{cathode} was measured using a teflon-coated T-type thermocouple. This junction was embedded inside a hole with a diameter of 1.4 mm and depth of 2.5 mm drilled in the top plane of the cathode. The hole was located on the centerline and near the downstream end of the cathode (see Fig. S6 below for the exact position). The thermocouple junction was fixed at the bottom of the hole filled with a heat-conductive resin.

Calculation of heat removed by the working liquid

The rate of heat removal by the working liquid Q was calculated from the power consumption of the ceramic heater measured by the power meter (Model 3333, Hioki) minus the amount of the heat escaped from the cell surface to the ambient air. The latter was obtained using a pre-calibrated relationship between the surface temperatures and the steady-state power consumption in the ceramic heater with $G = 0$ (i.e., no liquid flow). It should be noted that we did not calculate Q using $Q = \rho \times G \times C \times (T_{out} - T_{in})$, where ρ and C are the density and specific heat of the working liquid, respectively. Although this process also yielded quantitatively similar values to those obtained by the aforementioned method, we did not adopt the latter approach because we found that the multiplication of the four factors on the right-hand side of this relation caused intolerably large errors.

UV-vis optical absorption spectrum of the working liquid

Figure S1 shows the optical absorption spectrum of the working liquid (0.06 M solution of $Co^{II/III}(bpy)_3(NTf_2)_{2/3}$ in $[C_2mim][NTf_2]$) prepared using $Co^{II/III}(bpy)_3(NTf_2)_{2/3}$ supplied by Nippon Kayaku, Japan (black curve). To check the quality of the redox couple, we also purchased $Co^{II/III}(bpy)_3(NTf_2)_{2/3}$ from a different supplier (Dyenamo, Sweden) and compared the optical absorption spectrum of the solution (pink dashed curve) with that used in this report. Figure S1 shows that the agreement between these two spectra was excellent in terms of both the spectral shape and quantitative absorbance values, supporting the high purity of the redox couple used in this report.

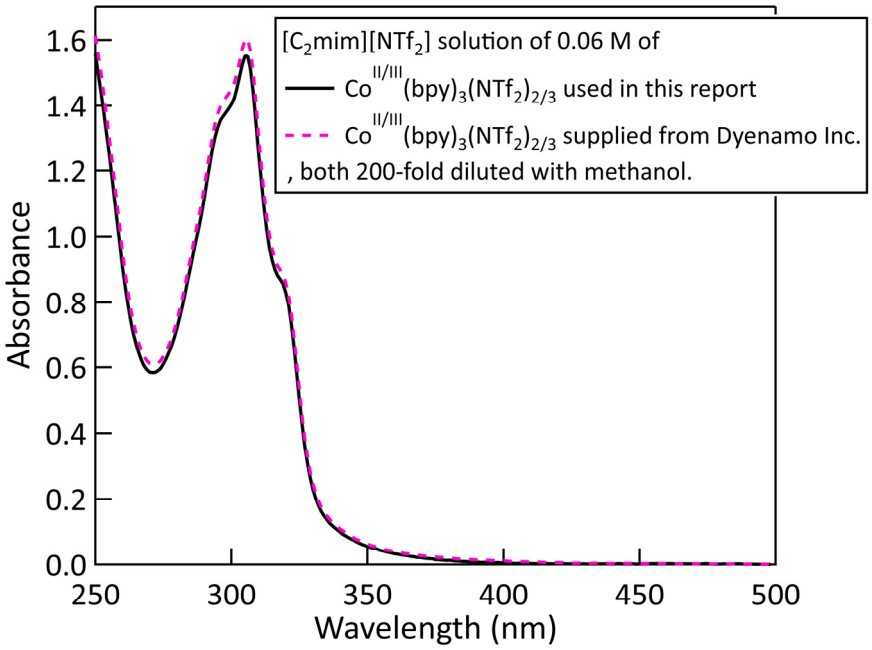

Fig. S1 Optical absorption spectrum of the working liquid (0.06 M solution of $Co^{II/III}(bpy)_3(NTf_2)_{2/3}$ in $[C_2mim][NTf_2]$) used in this report (black curve) compared with that of a working liquid prepared using $Co^{II/III}(bpy)_3(NTf_2)_{2/3}$ purchased from a different supplier (Dyenamo, Sweden; pink dashed curve). Both spectra were measured after 200-fold dilution with methanol. The optical path length was 1 mm.

UV-vis optical absorption spectrum of [C_2mim][NTf_2]

Figure S2 shows the optical absorption spectrum of the ionic liquid used in this report, [C_2mim][NTf_2] supplied from IoLiTec, Germany (see also Section 2 in the main text). The observed weak optical absorption in the UV region and the absence of absorption in the visible region supported the high purity of [C_2mim][NTf_2] certified by the supplier (> 99.5%). All optical absorption measurements in this report were conducted using a UV–vis–near-infrared spectrophotometer (UV-3600, Shimadzu) with a 1 mm-thick quartz cell.

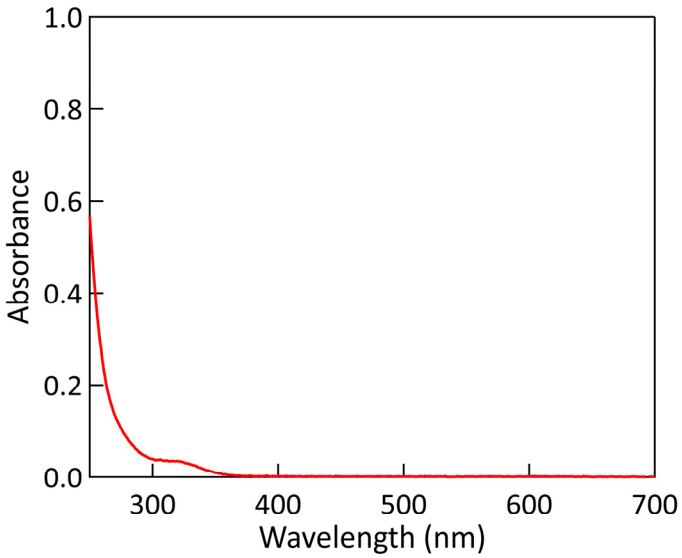

Fig. S2 Optical absorption spectrum of [C_2mim][NTf_2] used in this report. The optical path length was 1 mm.

Physical properties of [C_2mim][NTf_2]

Table S1 summarizes the physical properties of [C_2mim][NTf_2] relevant to the present study from 20 to 180 °C, which covers the entire temperature range used in this study. In Table S1, "Fit to eqn" means that these values were obtained using the fitting function shown in the footnote of

this table. In the simulations, temperature-dependent viscosity experimentally measured by us (shown in Table S2) was used along with the ρ, c_p, and k values stated in this table.

Table S1. Temperature dependence of the physical properties of [C2mim][NTf2]

Temperature, T (K)	Density, ρ (kg/m^3)		Specific heat, c_p (J/kg·K)		Thermal conductivity, k (W/m·K)		Viscosity, μ (mPa·s)	
	Experiment[a]	Fit to eqn[a,b]	Experiment[c]	Fit to eqn[c,d]	Experiment[e]	Fit to eqn[e,f]	Experiment[g]	Fit to eqn[g,h]
293.15 [20 °C]	1525.0	1524.2	1165.32	1172.21	0.1202	0.1203	41.6	40.7
303.15 [30 °C]	1515.1	1513.5	1193.43	1190.46	0.1215	0.1201	27.3	26.9
313.15 [40 °C]	1505.3	1503.0	1211.32	1208.70	0.1195	0.1198	19.1	18.8
323.15 [50 °C]	1495.5	1492.5	1226.65	1226.95	0.1184	0.1195	14.4	13.9
333.15 [60 °C]	1485.8	1482.1	1244.54	1245.19	0.1190	0.1193	11.3	10.6
343.15 [70 °C]	1476.1	1471.8	–	1263.44	0.1194	0.1190	8.3	8.4
353.15 [80 °C]	1466.4	1461.5	–	1281.68	0.1191	0.1187	6.8	6.8
373.15 [100 °C]	1447.0	1441.2	–	1318.17	–	0.1182	4.8	4.7
393.15 [120 °C]	1427.4	1421.2	–	1354.66	–	0.1177	3.7	3.5
413.15 [140 °C]	1407.5	1401.5	–	1391.15	–	0.1172	–	2.8
433.15 [160 °C]	1387.3	1382.0	–	1427.64	–	0.1166	–	2.2
453.15 [180 °C]	1366.6	1362.8	–	1464.13	–	0.1161	–	1.9

[a] M. Tariq et al., *Fluid Phase Equilibria*, 2010, **294**, 131–138.
[b] $\rho = 1000 \times \exp(0.62639 - 6.991512 \times 10^{-4}\ T)$
[c] E. Gómez et al., *Ind. Eng. Chem. Res.*, 2013, **52**, 2103–2110.
[d] $c_p = 637.36 + 1.8245\ T$
[e] A. P. Fröba et al. *Int. J. Thermophys.*, 2010, **31**, 2059–2077.
[f] $k = 0.1281 - 2.65 \times 10^{-5}\ T$
[g] A. Hofmann et al., *J. Chem. Eng. Data*, 2016, **61**, 114–123.
[h] $\mu = 1.82 \times 10^{-4} \times \exp(654.36/(T - 172.2))$.

Setup of the cell in the holder

The cell was suspended in the air using a holder made of aluminum to reproducibly suppress the physical contact between the cell unit and the surrounding environment. The cell unit was lifted up from the inner bottom of the "holder (bottom)" by a few millimeters using four PTFE screws ("lifting screws" in the side view of Fig. S3b) that penetrated from the bottom of the "holder (bottom)". The "holder (top)" was used to apply a downward force onto the thermal insulator and the ceramic heater so that the latter closely contacted the top plane of the cathode. By tightening the three plastic screws ("tightening screws" in Figs. S3a and b) that penetrated the "holder (top)"

plate, a downward force was applied constantly to the thermal insulator, affording a thermal contact between the heater and cathode during experiments.

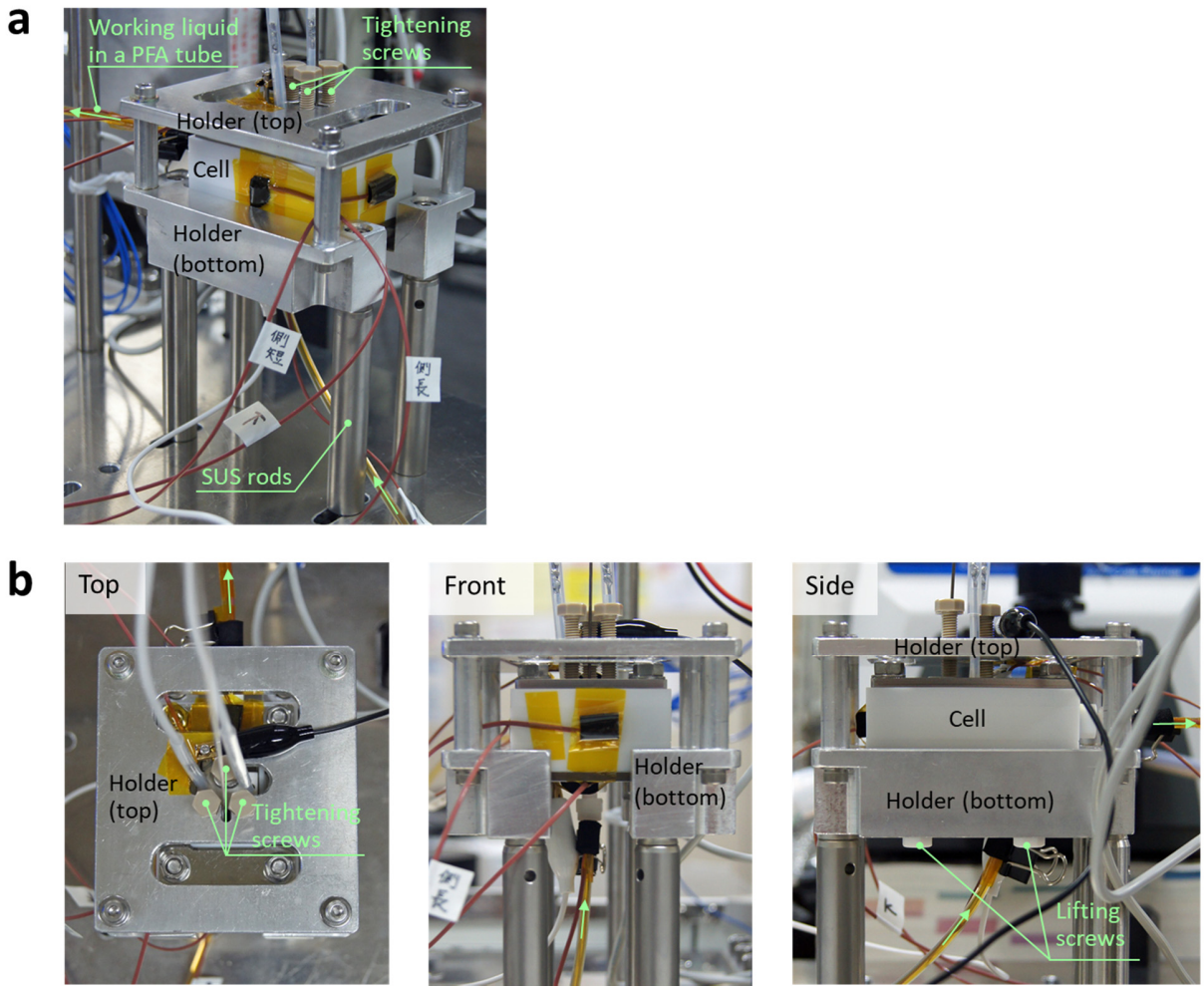

Fig. S3 (a) A photograph of the cell in an aluminum holder mounted on four 0.5″-diameter SUS rods. (b) Photographs of the top (left), front (middle), and side (right) of the setup. The photographs in (a) and (b) were taken during an experiment. Light-green arrows indicate the flow direction and the brown wires are teflon-coated thermocouple wires.

SMU settings

We found that proper choice of the measurement parameters in the source measure unit (SMU) was important for acquiring sound *I-V* curves. In particular, we found that improper choice of the parameters can cause artifacts, which are falsely better *I-V* curves and higher generated powers. Therefore, we present here the settings of the SMU used in this report. The SMU used in this study was a Model 2450 from Keithley. This SMU has two main parameters, "filter count (FC)" and "number of power line cycles (NPLCs)" that set the signal averaging time. As these values become larger, the time to complete an acquisition of one *I-V* curve becomes longer.

Figure S4 shows the dependences of P_{max} acquired in preliminary experiments carried out at G = 0.12 and 0.45 mL/s on the values of NPLCs and FC. The choice of small FC and NPLCs resulted in a falsely larger P_{max}, which was presumably caused by the transient current due to insufficient achievement of the steady state of the electrode reactions. Throughout this report, we used NPLCs = 10 and FC = 50, with which the steady state of the electrode reactions was sufficiently achieved and aforementioned artifacts could be avoided.

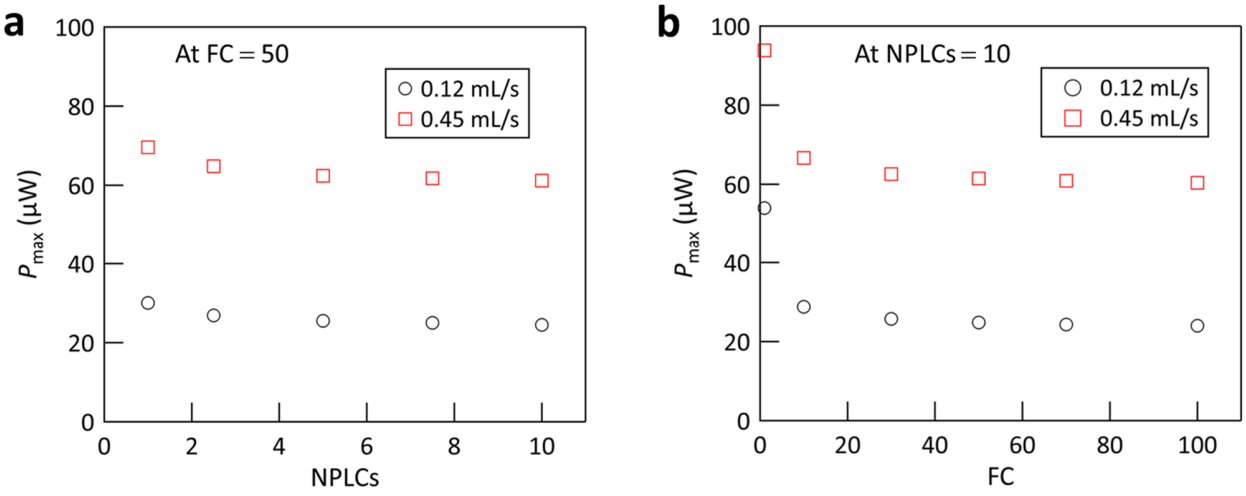

Fig. S4 Dependence of P_{max} obtained from the *I-V* curves acquired using the SMU on the parameters of (a) NPLC and (b) FC measured under FC = 50 and NPLCs = 10, respectively, at flow rates of 0.12 (circles) and 0.45 mL/s (squares).

3. Cross-sectional view of the computational graphic of the cell

Figure S5 shows the cross-sectional graphic of the cell used in this report with the computational meshes employed in our simulations for cathode #1. This computational graphic reflects the actual structure and dimensions of the present cell. Figure S5a also shows the position of the thermocouple hole in the cathode. Figure S5b indicates the position of $T_{channel,in}$. Figure S5c shows the color-contour map on the center cross section obtained from our simulation with $T_{cathode}$ = 170 °C and G = 0.5 mL/s.

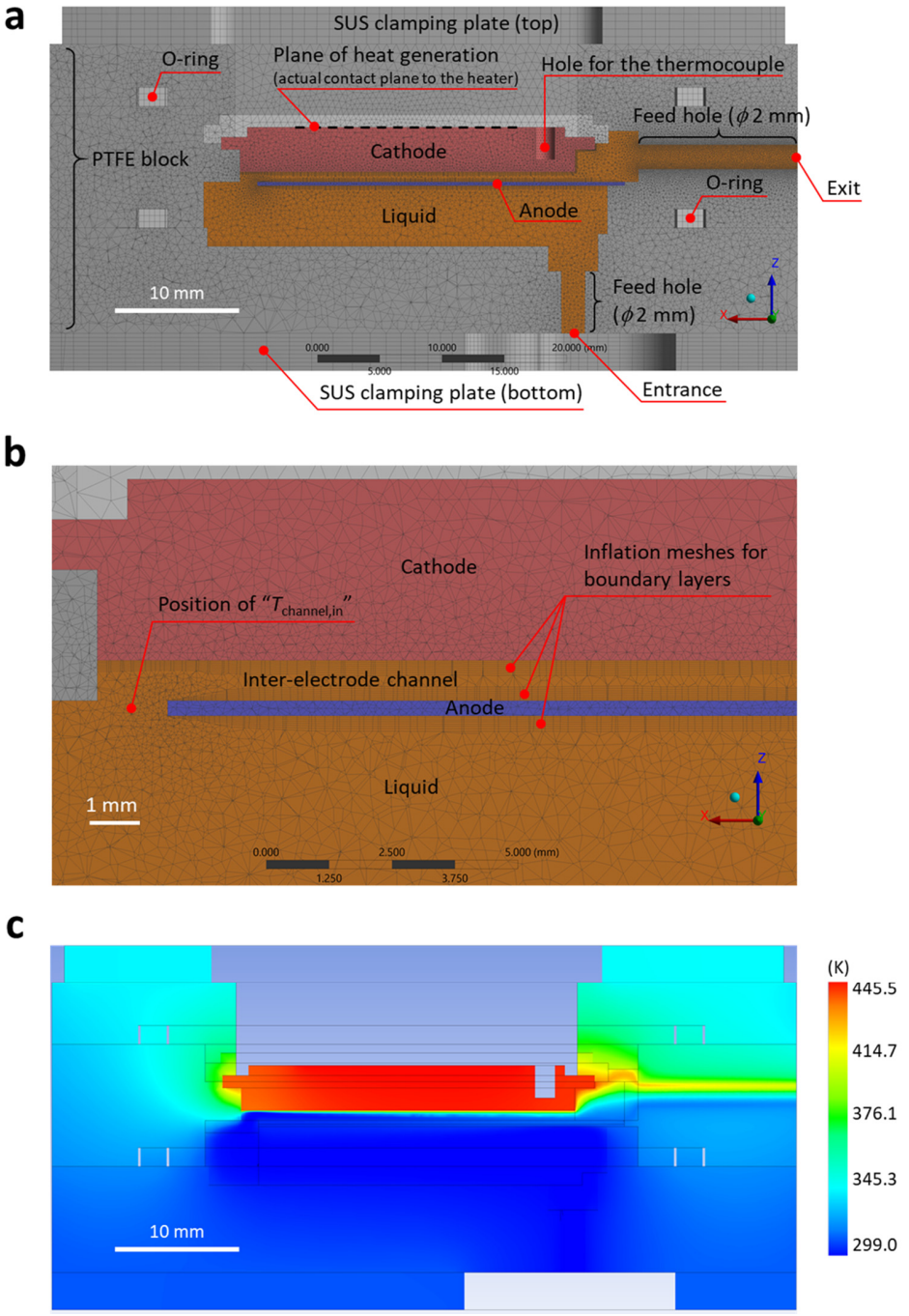

Fig. S5 Graphic of the cross section of the cell unit showing the meshes used in our simulations for cathode #1. This cross section is on the center plane of the cell cut parallel to the direction of the liquid flow. (a) The whole cross-section, (b) a magnified view around the entrance of the interelectrode channel, and (c) the temperature color-contour plot on the same cross section for T_{cathode} = 170 °C and G = 0.5 mL/s. In panel (b), the position of $T_{\mathrm{channel,in}}$ is indicated.

4. Theoretical basis for the use of narrow channel widths

A hydraulic diameter (D_h) is often used in evaluations of convection heat transfer.[S2,S3] D_h of a rectangular duct with cross-sectional dimensions of $a \times b$ is $2ab/(a + b)$.[S2] In the case of forced convection cooling using a laminar flow in a channel, the heat transfer coefficient h (W/(m^2·K)) is inversely proportional to D_h of the channel. This is because the Nusselt number ($Nu = hD_h/k$, where k is the thermal conductivity of fluid)[S2] for a fully developed flow is almost constant (usually somewhere between 3.5 and 4.5) regardless of the boundary conditions and the channel cross-sectional geometry.[S2,S3] Therefore, the easiest method to enhance h is to decrease D_h; this is the concept used in microchannel heat sinks, as mentioned in the main text.

A high h corresponds to a thin thermal boundary layer on a solid wall, which is a spatially steep temperature gradient in the liquid flowing along the wall.[S2] Such thin thermal boundary layers are beneficial for establishing a large steady-state temperature difference between two closely spaced electrodes in the present study (cf. Fig. 3 in the main text). For the same liquid flow rate (G), the use of cathode #1 results in a higher liquid velocity in the interelectrode channel than that in the case when cathode #2 is used because of the smaller cross-sectional area of the former than that of the latter, which also contributes to the formation of a thin thermal boundary layer in the case of cathode #1. Therefore, the use of cathode #1 is expected to result in a higher h and thus a higher heat removal rate than the use of cathode #2; this expectation was proven by the results shown in Figs. 4a and b in the main text. However, as a side effect of the smaller D_h, the cell with cathode #1 is expected to experience a larger pressure drop (ΔP) than the case for the cell with cathode #2. For the same G, a larger ΔP results in a larger pumping work ($G\Delta P$ (W)) necessary to force the liquid through the cell. This point is discussed in Section 3.5 of the main text.

5. Assessment of temperature non-uniformity on the cathode surface

Here we assess the extent of the temperature non-uniformity on the liquid-contacting plane of the cathode based on a theoretical analysis and computational simulation. We carry out a simulation for the cell with cathode #1 at G = 0.5 mL/s and $T_{cathode}$ = 170 °C, corresponding to the conditions that gave the maximum temperature non-uniformity in cathode #1. Figure S6 presents the simulated temperature distribution on the liquid-contacting plane of the cathode. This figure indicates that the temperature variation over most of the area (corresponding to the colors between red and light green) falls within ca. 6 K, or ca. ±3 K around the temperature at the thermocouple position (which is in the orange region in the color contour plot). This non-uniformity was sufficiently smaller than the temperature difference between the cathode and anode (ca. 130 K for these conditions; see the main text for details). Therefore, we assume that the temperature of the cathode can be represented by the temperature measured by the thermocouple embedded in the cathode throughout this report.

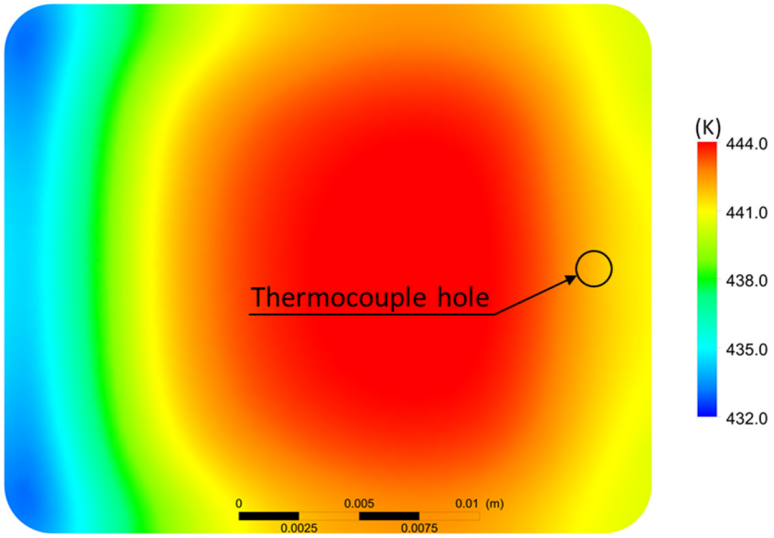

Fig. S6 Simulated temperature distribution on the liquid-contacting plane of cathode #1 for $T_{cathode}$ = 170 °C and G = 0.5 mL/s. In this graphic, the liquid flow was from left to right. The position of the hole for the thermocouple used to measure $T_{cathode}$ is indicated by a circle.

6. Temperature dependence of the viscosity of the working liquid

The temperature dependence of the viscosity of the working liquid was measured using a cone-plate rheometer equipped with a thermoelectrically controlled temperature stage (R/S Plus, Brookfield). The measurements were carried out under dry nitrogen gas to avoid the effect of moisture on the viscosity of the working liquid. Figure S7 shows the results along with the theoretical fit by the Vogel–Fulcher–Tammann (VFT) equation[S6]

$$\eta(T) = A \exp\left(\frac{B}{T-C}\right), \quad \text{(S5)}$$

where A, B, and C are the parameters. Our fit yielded $A = 7.2 \times 10^{-4}$ Pa·s, $B = 496.4$ K, and $C = 179.7$ K. These parameters were used to calculate the viscosity of the working liquid in our simulations. It should be noted that the viscosity obtained in Fig. S7 was higher than that of the neat [C_2mim][NTf_2] ionic liquid.

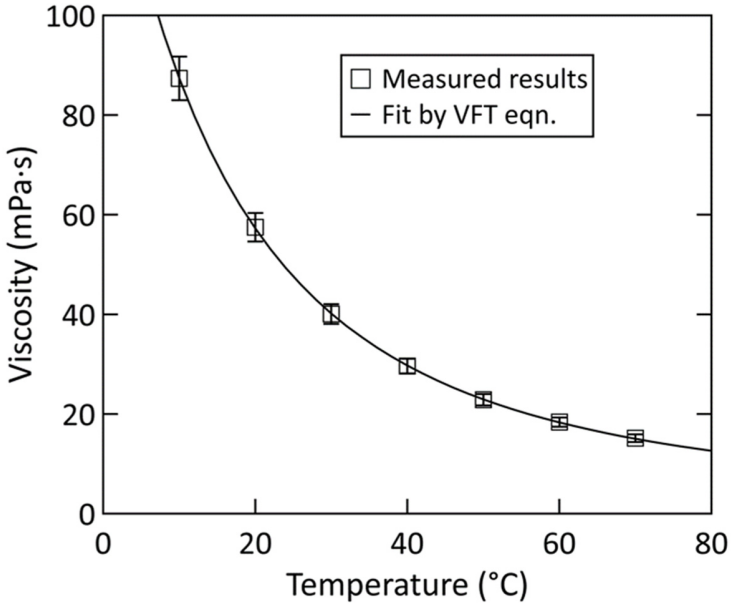

Fig. S7 Temperature dependence of the viscosity of the working liquid used in this report measured under dry nitrogen gas. The error bars represent ±5% uncertainty in the measurements. The black curve is a theoretical fit by the VFT equation.

Table S2 shows the temperature dependence of the viscosity from 20 to 180 °C. The values of "Fit to eqn" were obtained using eqn (S5) along with the VFT parameters obtained above.

Table S2. Temperature dependence of the viscosity of the working liquid

Temperature, T (K)	Viscosity, η (mPa·s)	
	Experiment[a]	Fit to eqn[b]
293.15 [20 °C]	57.47	57.3
303.15 [30 °C]	40.06	40.2
313.15 [40 °C]	29.61	29.7
323.15 [50 °C]	22.85	22.9
333.15 [60 °C]	18.38	18.3
343.15 [70 °C]	15.13	15.0
353.15 [80 °C]	–	12.6
373.15 [100 °C]	–	9.4
393.15 [120 °C]	–	7.4
413.15 [140 °C]	–	6.0
433.15 [160 °C]	–	5.1
453.15 [180 °C]	–	4.4

[a] See Fig. S7.
[b] $\eta = 7.21 \times 10^{-4} \times \exp(496.37/(T - 179.7))$, which is eqn (S5).

7. Simulation details

Boundary conditions

The boundary conditions used for the outer surface of the cell unit were as follows:

Natural convection — Heat transfer coefficients for the natural convection towards ambient air (23 °C) were estimated using the experimental correlation equations reported by S. W. Churchill and H. H. S. Chu, *Int. J. Heat and Mass Trans.*, 1975, **18**, 1323–1329 for vertical planes and W. H. McAdams, "Heat Transmission, 3rd ed.", McGraw-Hill, 1954; Chapter 7 for horizontal planes.

Thermal radiation — Emissivity values of 0.7 and 0.15 were used for PTFE and stainless-steel surfaces, respectively. The temperature of the surrounding environment was 23 °C.

Model type and settings

The following model type and settings of Fluent® were used for the simulations:

Type = pressure-based

Velocity formulation = absolute

Gravity = ON (–9.8 m/s^2)

Multiphase = OFF

Energy = ON

Viscous = laminar

Solidification & melting = OFF

Electric potential = OFF

Grid independence study

To show that our simulation results were independent of the density of the grid (or mesh) used, we carried out a grid independence study. As shown in Fig. S8, the results of our simulations were independent of the mesh density.

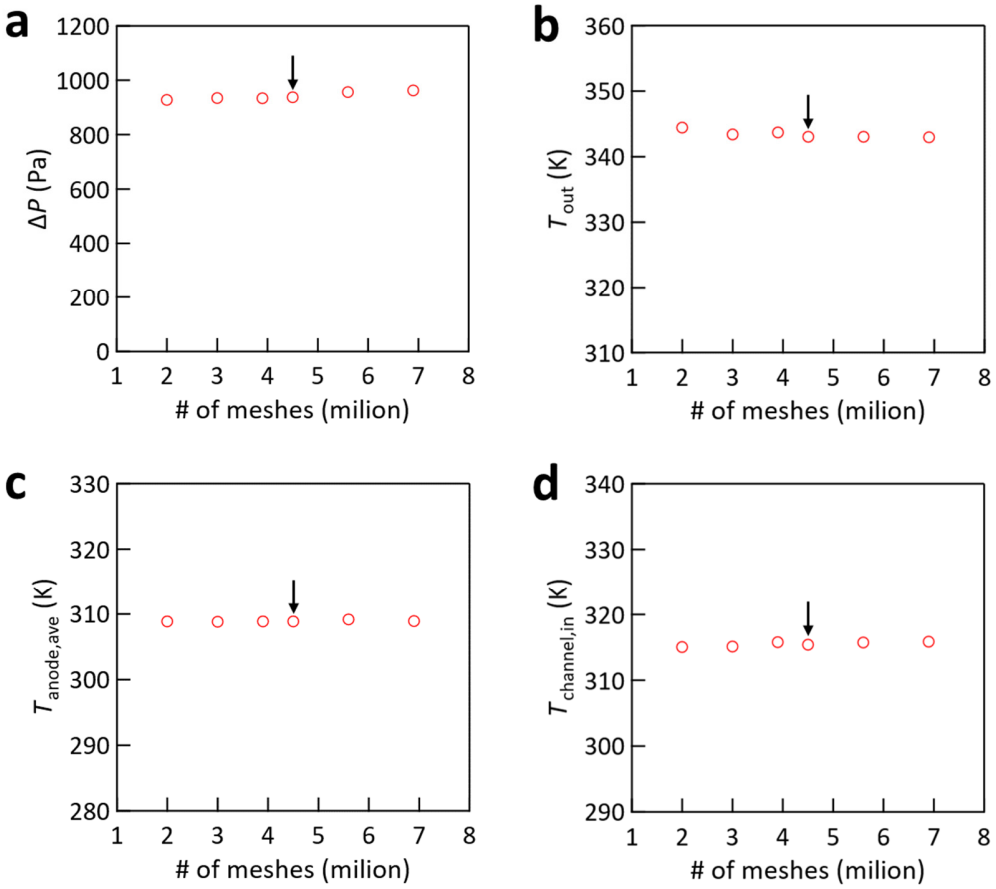

Fig. S8 Results of the grid independence study for the simulations in this report for (a) ΔP, (b) T_{out}, (c) $T_{\text{anode,ave}}$, and (d) $T_{\text{channel,in}}$. For definitions of the symbols used here, refer to the main text. Downward arrows indicate the mesh condition used in this report (4.5 million mesh).

Governing equations

The governing equations for the simulations in this report are listed below:

Mass conservation law: $\nabla \cdot (\rho \vec{u}) = 0$

Momentum conservation law: $\nabla \cdot (\rho \vec{u}\vec{u}) = -\nabla p + \nabla \cdot (\bar{\bar{\tau}}) + \rho \vec{g}$

Energy conservation law: $\rho c_{\text{p}} \vec{u} \cdot \nabla T = \nabla \cdot (k \nabla T)$

Here, ρ is density, $\vec{u}$ is the velocity vector, p is static pressure, $\bar{\bar{\tau}}$ is the stress tensor, $\vec{g}$ is the gravity vector, μ is viscosity, c_p is specific heat, and k is thermal conductivity.

8. Derivation of the small-signal mass transfer resistance R_{mt}

Full details of a semi-empirical model for steady-state mass transfer have been given in Section 1.4 of a textbook by Bard and Faulkner.[S4] In this model, a redox reaction on the electrode surface $O + ne \leftrightarrow R$ (O: oxidized form; R: reduced form; n: the number of electrons involved) is considered for the situation where a steady-state flow of an electrolyte parallel to the electrode plane (which may be caused by stirring or forced convection) has formed a Nernst diffusion layer on the electrode,[S4] as depicted in Fig. S9. This figure depicts an example situation of a reaction $O + ne \rightarrow R$ where the electrode is a cathode. The concentration of the redox species (O in this case) outside the diffusion layer of thickness δ_O is maintained at the bulk concentration (C_O^*) because

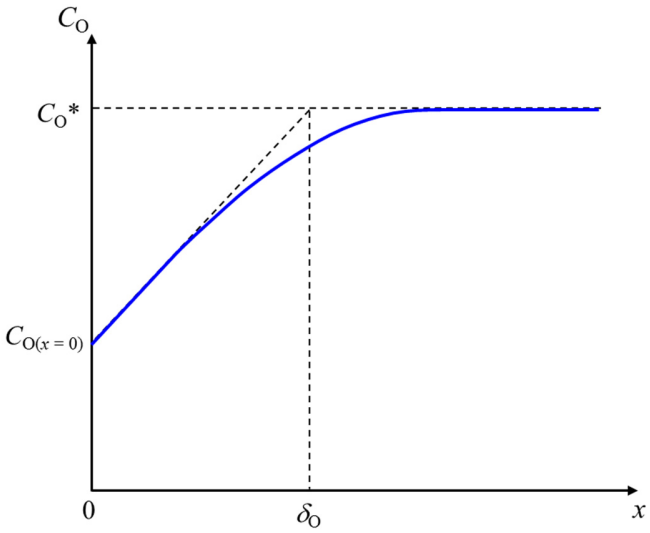

Fig. S9 Concentration profile for species O near the electrode. The electrode surface is $x = 0$. The solid curve represents the concentration profile and the dashed lines represent the diffusion layer approximation. δ_O and $C_{O(x=0)}$ are the diffusion layer thickness and concentration of O on the electrode, respectively. This figure was drawn based on Figure 1.4.1 of ref. S4.

of the steady flow of the electrolyte, whereas the concentration on the electrode surface ($C_{O(x=0)}$) is lower than C_O* because of the steady consumption of O by the Faradaic reaction occurring at the electrode. C_O varies with the distance (x) from the electrode in the diffusion layer.

Because the details of this mass transfer model have been described elsewhere,[S4] here we only briefly introduce this model to derive a solution (eqn (3) in the main text). First, the current–potential (I-E) relationship for the case where both O and R are present initially is given by[S4]

$$E = E^{0\prime} - \frac{RT}{nF}\ln\left(\frac{m_O}{m_R}\right) + \frac{RT}{nF}\ln\left(\frac{I_{lim,c}-I}{I-I_{lim,a}}\right), \quad \text{(S6)}$$

where $E^{0\prime}$ is the formal potential, R is the gas constant, T is the absolute temperature, F is the Faraday constant, $I_{lim,c}$ is the cathodic limiting current, and $I_{lim,a}$ is the anodic limiting current. Here, the variables m_X (X: O or R) are defined by

$$m_X \equiv \frac{D_X}{\delta_X}, \quad \text{(S7)}$$

where D_x is the diffusion coefficient of species X. In eqn (S6), the signs of $I_{lim,c}$ and $I_{lim,a}$ are defined to be opposite to each other.[S4] From eqn (S6), the equilibrium potential E_{eq}, which is the potential at $I = 0$, can be expressed by

$$E_{eq} = E^{0\prime} - \frac{RT}{nF}\ln\left(\frac{m_O}{m_R}\right) + \frac{RT}{nF}\ln\left(-\frac{I_{lim,c}}{I_{lim,a}}\right), \quad \text{(S8)}$$

Then, the mass transfer overpotential η_{mt} can be expressed as[S4]

$$\eta_{mt} = E - E_{eq} = \frac{RT}{nF}\ln\left(\frac{I_{lim,c}-I}{I-I_{lim,a}}\right) - \frac{RT}{nF}\ln\left(-\frac{I_{lim,c}}{I_{lim,a}}\right). \quad \text{(S9)}$$

As a result of the subtraction in eqn (S9), the parameters m_X (and thus D_X and δ_X) are eliminated from this equation. For the conditions of small deviations of E from E_{eq} (i.e., $E \cong E_{eq}$), the *"small-signal" mass transfer resistance* R_{mt}[S4] can be defined as

$$R_{mt} \equiv \left(\frac{\partial \eta_{mt}}{\partial I}\right)_{I=0}. \quad \text{(S10)}$$

By substituting eqn (S9) into eqn (S10), R_{mt} is obtained as follows

$$R_{mt} = \frac{RT}{nF}\left(\frac{I_{lim,a}-I_{lim,c}}{I_{lim,a}I_{lim,c}}\right). \quad \text{(S11)}$$

Equation (S6) is the representation for the situation of Fig. S9 and thus the terms "$I_{lim,c}$" and "$I_{lim,a}$" have been defined for one electrode. However, in the present forced-flow thermocell, because the mass transfer resistance contained contributions from both the cathode and anode, an overall R_{mt} has to be determined. To consider this point, the pair of terms representing the two limiting currents above ($I_{lim,c}$ and $I_{lim,a}$) are replaced by a new pair of terms, $I_{lim,forward}$ and $I_{lim,backward}$. Here, "$I_{lim,forward}$" is the limiting current found from Figs. 5d and 6a in the main text, where our "cathode" and "anode" literally work according to their names. Conversely, "$I_{lim,backword}$" is the limiting current that would be measured when our "cathode" and "anode" work as an anode and cathode, respectively; i.e., when the current flows inversely to the intended design by applying an inverse potential between the electrodes. Using the SMU, such an inverse measurement was possible. Figure S10 shows the *I-V* curves acquired for the normal and inverse scans obtained using cathode #2 with $T_{cathode}$ = 170

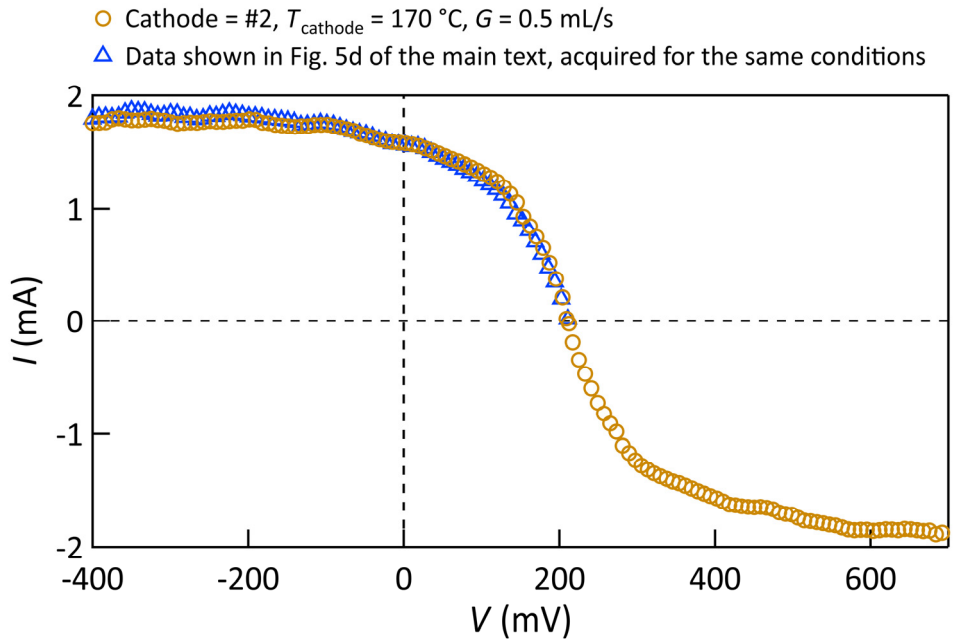

Fig. S10 *I-V* curves acquired by scans in both the normal and inverse directions using cathode #2 with $T_{cathode}$ = 170 °C and G = 0.5 mL/s (circles). These normal and inverse scans were carried out on the same day. As a comparison, the *I-V* curve scanned only for the normal direction for the same experimental conditions is also shown (triangles), which is also presented in Fig. 5d of the main text. The acquisition of the former was carried out a few months later than that of the latter, demonstrating the high reproducibility of the experimental results.

°C and G = 0.5 mL/s. Figure S10 shows that $I_{\mathrm{lim,backward}}$ was equal to $-I_{\mathrm{lim,forward}}$ in the present cell, and therefore the following relation can be used for the present situation

$$I_{\mathrm{lim,forward}} \cong -I_{\mathrm{lim,backward}} \equiv I_{\mathrm{lim}} \ (> 0). \tag{S12}$$

By substituting eqn (S12) into eqn (S11), R_{mt} can be expressed as

$$R_{\mathrm{mt}} \cong \frac{RT}{nF}\frac{2}{I_{\mathrm{lim}}}, \tag{S13}$$

which is eqn (3) in the main text.

Next, the reason for the factor "2" in eqn (S13) is briefly mentioned. As stated in the main text, R_{mt} in this work is the *overall* mass transfer resistance containing contributions from diffusion layers on both the cathode and anode. However, the factor "2" in eqn (S13) did not originate from this aspect. The essential feature of eqn (S6) is that the magnitude of R_{mt} near $E \cong E_{\mathrm{eq}}$ (or $I \cong 0$) contains contributions from both the limiting current for the forward reaction and that for the reverse reaction when the reduced and oxidized species coexist in a liquid electrolyte.[S4] Therefore, the factor "2" in eqn (S13) originates from the relationship in eqn (S12).

As briefly mentioned in the main text, Abraham et al.[S5] previously used the same theoretical framework in their report to obtain R_{mt} but they followed a different route from ours presented above. In their route, I_{lim} was calculated using

$$|I_{\mathrm{lim}}| = \frac{nFADC}{\delta}, \tag{S14}$$

which is equation (1.4.17) in the textbook authored by Bard and Faulkner.[S4] Specifically, Abraham et al.[S5] used the value of D separately obtained from their experiments while treating δ as an adjustable parameter in eqn (S14). In our case, I_{lim} was obtained experimentally and thus it was not necessary to use D or δ in our route described above. We believe that both routes are equally

important because one can choose to use whichever is the better route depending on the available experimental data.

Back to our analysis, eqn (S9) can be rewritten using eqn (S12) as

$$E = E_{\mathrm{eq}} + \frac{RT}{nF} \ln\left(\frac{I_{\mathrm{lim}} - I}{I_{\mathrm{lim}} + I}\right), \qquad \text{(S15)}$$

which describes the relationship between the voltage and current as a function of I_{lim}. An example of the fit to the experimental *I*-*V* curves in Fig. 6a of the main text with eqn (S15) is shown in Fig. S11. Further discussion and analyses of eqn (S15) are beyond the scope of the present report.

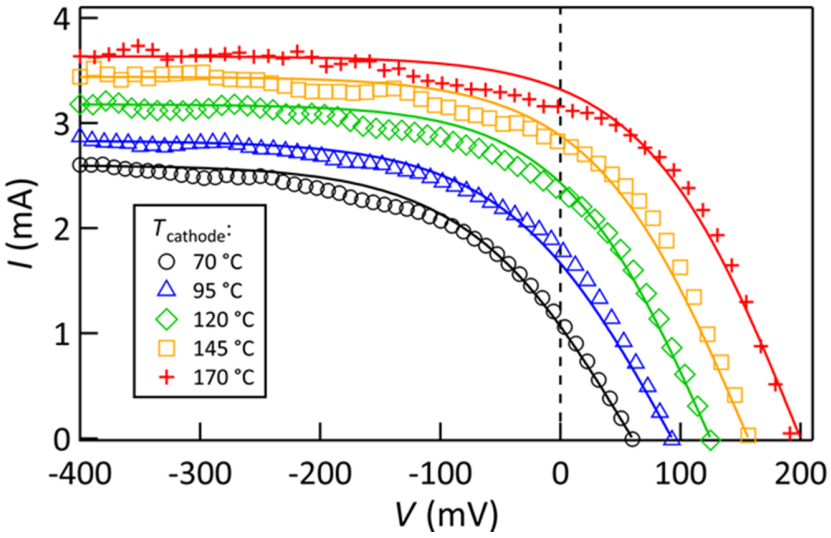

Fig. S11 Example fits of eqn (S15) to the *I*-*V* curves shown in Fig. 6a of the main text.

9. Arrhenius plots of the working liquid viscosity and R_{ct}^{-1}

Figures S12a and b show two Arrhenius plots to support the discussion in the main text. Figure S12a is the Arrhenius plot for the viscosity of the working liquid, which was generated from our data presented in Fig. S7. The slope represents the activation energy of the viscosity, $E_{a(\eta)}$. Figure S12b is the Arrhenius plot for the inverse of R_{ct} (data shown in Fig. 6d of the main text), where the slope represents the apparent activation energy.[S7] For the temperature for the latter, the average temperature of $T_{cathode}$ and $T_{anode,ave}$ was used, where $T_{anode,ave}$ was obtained from our simulations. In agreement with the results of Tachikawa et al.,[S7] who investigated the electrode kinetics of several ion complexes in an ionic liquid similar to [C_2mim][NTf_2] used in the present report, these activation energies are similar to each other.

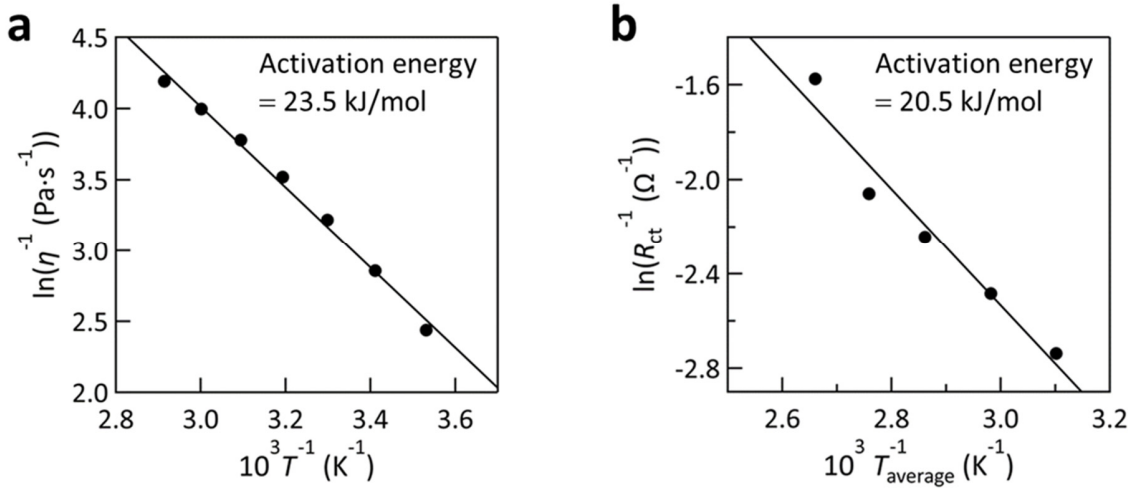

Fig. S12 Arrhenius plots of (a) the viscosity of the working liquid and (b) the inverse of R_{ct} obtained from the temperature-dependent experiments shown in Fig. 6 of the main text.

10. Dependence of $T_{anode,ave}$ on G

To support the explanation given for the increase of V_{OC} with increasing G found in Fig. 7a of the main text, corresponding simulations were carried out for the condition of $T_{cathode}$ = 170 °C. Figure S13 shows the simulated relation between $T_{anode,ave}$ and G. As expected, $T_{anode,ave}$ decreased with increasing G, supporting our explanation for the observed increase of V_{OC} with G in the main text.

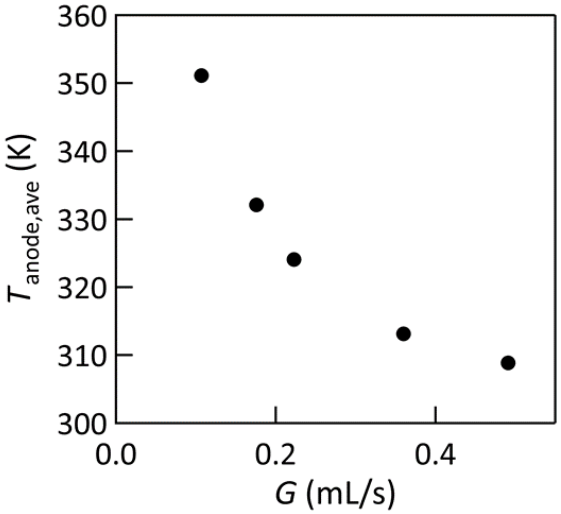

Fig. S13 Simulated $T_{anode,ave}$ vs. G for the experimental conditions in Fig. 7 in the main text.

11. Randles plots generated from the results of AC impedance measurements

Using the results of AC impedance measurements, plots of impedance vs. $\omega^{-1/2}$ (ω: AC frequency), often called Randles plots, can be generated. Randles plots are useful for analyzing the electrochemical processes.[S4] As described in Section 10.3 of ref. S4 as well as Section 3.4 of the main text, the slope of a Randles plot is related to the diffusion coefficient of the redox species in the solvent (eqn (4) in the main text). Figure S14 shows the Randles plots for different G generated from the data presented in Fig. 7d of the main text. In all the panels in Fig. S14, the plots for both the real (Z_{Re}) and imaginary (Z_{im}) components are linear and have a common slope, which indicates that the present system can be described by the equivalent circuit model.[S4]

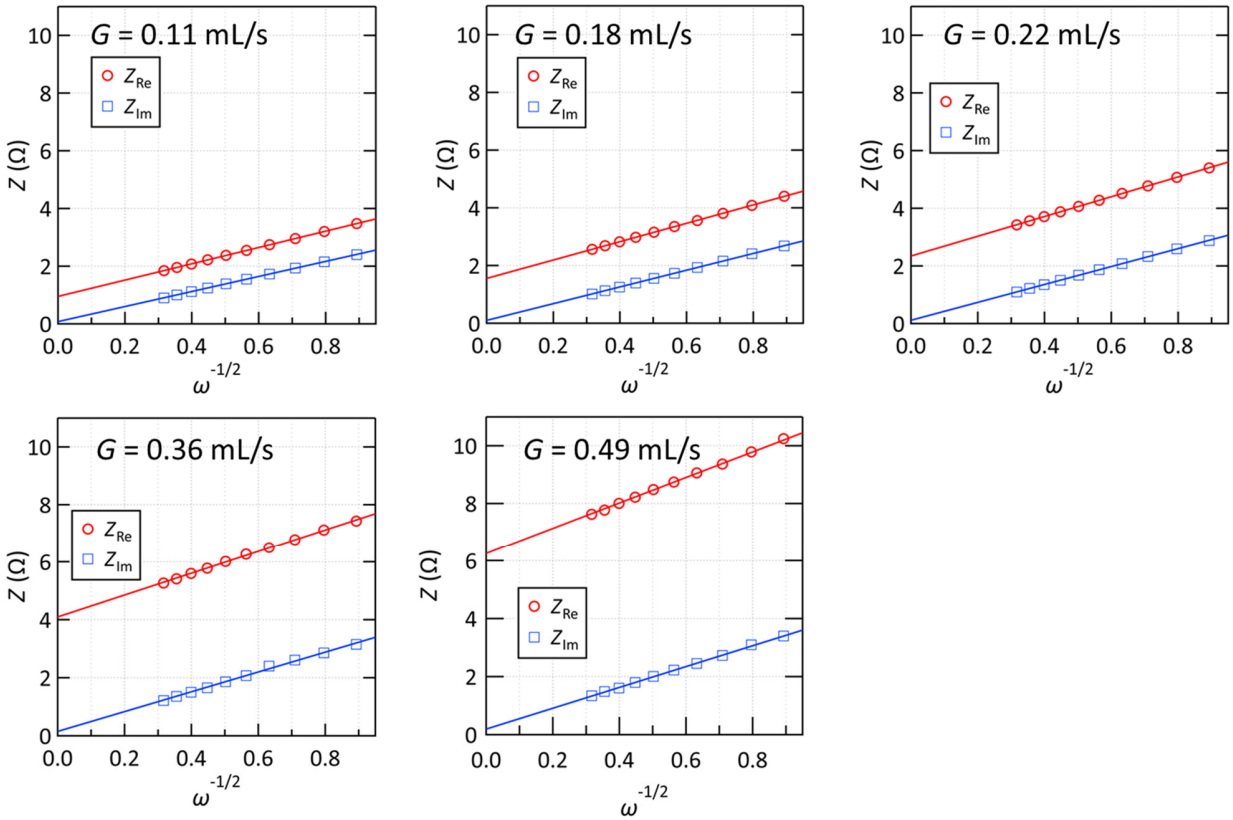

Fig. S14 Randles plots generated from the results of the AC impedance measurements shown in Fig. 7d of the main text.

References

(S1) Y. A. Cengel and M. A. Boles, *Thermodynamics —An Engineering Approach 7th Ed.*, McGraw-Hill, New York, 2011.

(S2) A. F. Mills, *Heat Transfer 2nd Ed.*, Prentice Hall, New Jersey, 1998.

(S3) M. A. Ebadian and Z. F. Dong, in *Handbook of Heat Transfer 3rd Edition*, ed. W. M. Rohsenow, J. P. Hartnett and Y. I. Cho, McGraw-Hill, New York, 1998, Chapter 5.

(S4) A. J. Bard and L. R. Faulkner, *Electrochemical Methods —Fundamentals and Applications 2nd Edition*, John Wiley & Sons, New York, 2000.

(S5) T. J. Abraham, N. Tachikawa, D. R. MacFarlane and J. M. Pringle, *Phys. Chem. Chem. Phys.*, 2014, **16**, 2527–2532.

(S6) G. W. Scherer, *J. Am. Ceram. Soc.*, 1992, **75**, 1060–1062.

(S7) N. Tachikawa, Y. Katayama and T. Miura, *J. Electrochem. Soc.*, 2007, **154**, F211–F216.